RESEARCH ARTICLE

Key Points:
- There is a significant interannual relationship between East African early short rains and boreal winter Arctic Oscillation
- Winter Arctic Oscillation induces anomalous wind stress curl in tropical Indian Ocean which generates oceanic Rossby waves
- Downwelling Rossby waves lead to anomalous upper ocean heat content which enhance precipitation over East Africa in October

Correspondence to:
D.-Y. Gong,
gdy@bnu.edu.cn

Interannual modulation of East African early short rains by the winter Arctic Oscillation

Dao-Yi Gong[1], Dong Guo[2], Rui Mao[1], Jing Yang[1], Yongqi Gao[3,4], and Seong-Joong Kim[5]

[1]State Key Laboratory of Earth Surface Processes and Resource Ecology, Beijing Normal University, Beijing, China, [2]Climate Change Research Center, Chinese Academy of Sciences, Beijing, China, [3]Nansen-Zhu International Research Center, IAP/CAS, Beijing, China, [4]Bjerknes Center for Climate Research, Nansen Environmental and Remote Sensing Center, Bergen, Norway, [5]Division of Polar Climate Change, Korea Polar Research Institute, Incheon, South Korea

Abstract In the present study, we analyzed the interannual linkage between the boreal winter Arctic Oscillation (AO) and East African early short rains. When the Indian Ocean Dipole and El Niño–Southern Oscillation variance are excluded by linear regression, the boreal winter AO index is significantly correlated with the October East African precipitation over the domain of 5°N–5°S and 35°–45°E for the period 1979–2014, $r = +0.46$. The upper ocean heat content likely acts as a medium that links the AO and East African precipitation. Significant subsurface warming and positive upper ocean heat content anomalies occur over the western Indian Ocean during the autumn following positive AO winters, which enriches the atmospheric moisture, intensifies convection, and enhances precipitation. Oceanic dynamics play a key role in causing this subsurface warming. Winter AO-related atmospheric circulation creates anomalous wind stress, which forces a downwelling oceanic Rossby wave between 60°–75°E and 5°–10°S, where the thermocline significantly deepens. This Rossby wave propagates westward and accompanies significant subsurface warming along the thermocline. The Rossby wave arrives at the western Indian Ocean in the late summer, significantly warming the region to the west of 55°E at a depth of 60–100 m. This warming remains significant through October. Correspondingly, the upper ocean heat content significantly increases by approximately $2–3 \times 10^8$ J m^{-2} in the region west of 60°E between 5° and 10°S. The role of these oceanic dynamics in linking the winter AO, and anomalous subsurface warming was tested by numerical experiments with an oceanic general circulation model. The experiments were performed with the forcing of AO-related wind stress anomalies over the Indian Ocean in the winter. The oceanic Rossby wave generated in the central Indian Ocean during boreal winter, the consequent subsurface warming, and the anomalous upper ocean heat content in October over the western Indian Ocean were all adequately reproduced. The winter AO can serve as a precursor of East African short rain anomalies.

1. Introduction

Equatorial East Africa exhibits two peaks of precipitation every year following the seasonal migration of the intertropical convergence zone. One peak occurs around March–May (i.e., long rains), and the other peak occurs from October to December (i.e., short rains). Although short rains bring less precipitation than long rains (Figure 1), the former have higher interannual variability with recurrent droughts and floods, such as those of 1997, 2005, and 2010 [e.g., *Hastenrath et al.*, 2007, 2010; *Liebmann et al.*, 2012; *Philippon et al.*, 2015]. Improving our understanding of the variability of short rains is important for the livelihood of millions. Previous studies have documented physically robust drivers that directly or indirectly modulate the East African short rains, which involve large-scale atmospheric and/or oceanic linkages. For example, *Hastenrath* [2000, 2007] and *Mutai et al.* [2012] emphasized the importance of the zonal vertical circulation cell along the Indian Ocean's equator, where an anomalous descending (ascending) western branch of the cell near approximately 40°E suppresses (enhances) the rainfall in East Africa. *Nicholson* [2015] indicated that this cell plays a strong role in producing wet conditions. *Manatsa et al.* [2014] reported that a westward displacement of the Mascarene High produces below normal sea surface temperatures (SSTs) in the southern Indian Ocean and that the suppressed convection over the western tropical Indian Ocean leads to below normal precipitation in East Africa. The southern annular mode may indirectly influence these short rains by modulating the Mascarene High [*Manatsa et al.*, 2015].
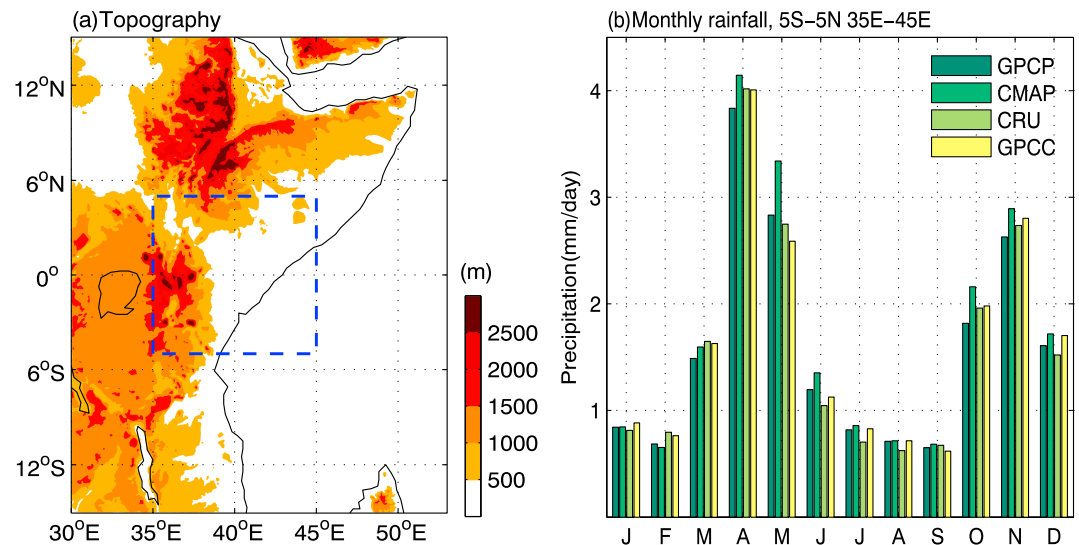
Figure 1. (a) Topography of East Africa, (b) long-term means of the monthly precipitation over the region of 5°S–5°N and 35°–45°E with respect to 1981–2010. Target region is shown as the box in Figure 1a).

Oceanic thermal/dynamical conditions play important roles in precipitation variability over East Africa. Observations and simulation analyses have demonstrated that the short rains exhibit a significant association with the El Niño–Southern Oscillation (ENSO). A warmer ENSO phase is often accompanied by a wetter short rain season in equatorial East Africa, whereas a colder phase is followed by drier conditions [e.g., *Hutchinson*, 1992; *Indeje et al.*, 2000; *Clark et al.*, 2003; *Preethi et al.*, 2015; among others]. Compared to the ENSO, the Indian Ocean Dipole (IOD), whose outstanding feature is a west-east contrast of SST anomalies, is suggested to significantly influence East Africa's short rains. Above average precipitation appears in the western Indian Ocean and neighboring East Africa following a positive SST anomaly in the western tropical Indian Ocean and a negative anomaly in the east [*Hastenrath et al.*, 1993; *Saji et al.*, 1999; *Webster et al.*, 1999]. The major role of the IOD in the variability of these short rains has been confirmed by numerical experiments [*Goddard and Graham*, 1999; *Latif et al.*, 1999; *Behera et al.*, 2005; *Bahaga et al.*, 2015]. This in-phase relationship between the SST and precipitation has also been reproduced in the 20th century ensemble simulations by 17 coupled ocean-atmosphere general circulation models [*Saji et al.*, 2006]. This relationship varies with time and has strengthened since the early 1960s [*Clark et al.*, 2003; *Manatsa and Behera*, 2013]. In addition to the basin-scale SST, the enhancement of East African short rains from local warm SST anomalies in the western equatorial Indian Ocean is particularly noteworthy [*Black et al.*, 2003; *Ummenhofer et al.*, 2009; *Liebmann et al.*, 2014].

The warming in the western Indian Ocean, which might be caused by the IOD/ENSO, anomalous atmospheric circulation, or remote factors outside the Indian Ocean, induces abundant short rains. Local/regional horizontal moisture transport is a key factor. For example, *Chan et al.* [2008] emphasized the importance of the moisture that is transported from the western Indian Ocean to East Africa. Accompanying these warmer SSTs over the western Indian Ocean near the East African coastline is an active center of vertical motion and deep convection, which induces this easterly moisture transport and favors precipitation during short rain seasons. *Ummenhofer et al.* [2009] indicated that warming in the western Indian Ocean creates lower pressure over the western Indian Ocean and neighboring East Africa. The low pressure in this region drives anomalous westerlies to the west and easterlies to the east, and the resultant convergence of this moisture transport creates above average precipitation over East Africa. Recently, *Bahaga et al.* [2015] indicated that a Gill-type response of the atmosphere to a warmer western Indian Ocean induces a low-level anomalous westerly over equatorial Africa, which creates moisture flux convergence over East Africa. In addition, the favorable moisture and circulation conditions in the tropical Indian Ocean may be maintained/amplified through positive feedback among the winds, thermocline, and SST gradient that enhances East African precipitation [*Webster et al.*, 1999].

There is evidence showing that the winter Arctic Oscillation (AO)/North Atlantic Oscillation (NAO) can influence the tropical climates over the western North Pacific and Indian Ocean on interannual timescale [e.g., *Gong et al.*, 2014, 2016]. In association with active AO during the boreal winter, the AO-related transient

eddy-mean flow interactions in the North Pacific generate anomalous dipole circulation with a cyclone to the southern side of the jet stream and an anticyclone to the north [*Gong et al.*, 2011]. Meanwhile, the upper troposphere over Eurasian continents is dominated by large-scale wave trains [*Branstator*, 2002; *Watanabe*, 2004]. Particularly, the southern Asian jet stream plays important roles in trapping the vorticity disturbances that originated from the middle to high latitudes and modulating its downstream propagation through waveguide effects over the Middle East and India. Consistently, the salient pattern over the northern Indian Ocean is an anomalous anticyclonic circulation which is dominant from middle to upper troposphere. In addition, the strong downward air motion enhances the lower troposphere Arabian High. Thus, from surface to middle troposphere there are significant northern winds flowing across the equator between 50° and 70°E. Three-dimensional circulation changes over Indian Ocean in association with boreal winter AO were analyzed in detail in *Gong et al.* [2014]. Anyway, this atmospheric teleconnection linking AO/NAO and intraseasonal to interannual Indian Ocean (particularly the tropical Indian Ocean) climates were documented with physical explanation by previous observation and simulation studies [*Lin et al.*, 2009; *Yuan et al.*, 2011; *Gong et al.*, 2014, among others].

In the present study, we present evidence that the East African early short rains are modulated by the boreal winter AO through a persistent anomaly in the upper ocean heat content and the atmospheric moisture and convection over the western Indian Ocean. The remainder of this paper is organized as follows. Section 2 describes the data and methods that are used in this study. Section 3 presents the statistical relationship between the winter AO and East African early short rains and then demonstrates the corresponding changes in the atmospheric circulation and humidity. Section 4 investigates the possible mechanisms that connect the winter AO and early short rains, with a focus on the upper ocean heat content and AO-related oceanic Rossby wave. Section 5 tests the role of the AO-forced oceanic dynamics by numerical experiments with an oceanic general circulation model. Finally, the major findings of this study are summarized in section 6.

2. Data and Methodology

2.1. Data

We used the AO and Niño 3.4 SSTs from the Climate Prediction Center (CPC, NOAA). Here the time series of the AO index was constructed by projecting 1000 hPa height anomalies poleward of 20°N onto the loading pattern of the AO mode. The AO is most active during January–February–March (JFM) [*Thompson and Wallace*, 2000], so we considered JFM to be the boreal winter in this study. The Niño 3.4 SST is the averaged SST anomalies over 5°N–5°S and 170°–120°W. The intensity of the IOD is represented by anomalous SST gradients between the western equatorial Indian Ocean (50°–70°E and 10°S–10°N) and the southeastern equatorial Indian Ocean (90°–110°E and 10°S–0°) [*Saji et al.*, 1999] and was computed by using the Extended Reconstructed Sea Surface Temperature data set (ERSST v3b). The Simple Ocean Data Assimilation (SODA) product version 2.2.4, which is updated to December 2010, was used to investigate the variations in the subsurface temperature, heat content, and sea surface height (SSH). The 20°C isotherm depth (D20) was calculated based on the SODA seawater temperature and was used as an indicator of the thermocline. The spatial resolution of SODA was 0.5°, and the resolution of the uppermost levels of the 40 total vertical layers was approximately 10 m [*Carton and Giese*, 2008]. The atmospheric circulation and humidity fields were taken from the ERA Interim reanalysis data set, which is available at 1.5° resolution.

Four monthly observational precipitation data sets were used in this study. The Global Precipitation Climatology Centre (GPCC v7) provides 1° gridded land precipitation estimates that are based solely on station data [*Schneider et al.*, 2014]. The second data set was the Global Precipitation Climatology Project's (GPCP v2.2) monthly precipitation data set, which combines observations and satellite precipitation data with a resolution of 2.5° [*Adler et al.*, 2003]. The third data set was the grid box monthly rainfall database from the Climate Research Unit (CRU TS323), which has a resolution of 0.5° [*Harris et al.*, 2014]. The fourth data set was the merged analysis of precipitation from CPC (CMAP), which has a resolution of 2.5° [*Xie and Arkin*, 1997]. The regional mean monthly precipitation was computed over the target area between 5°S–5°N and 35°–45°E (Figure 1) for each of these four data sets. In this study, these climate time series were confined to the period 1979–2014.

We computed the regional mean precipitation averaged over the domain of 5°N–5°S and 35°–45°E using the GPCC, GPCP, CRU, and CMAP data sets. Then these four time series were averaged into a single one, which was defined as the equatorial East African rainfall index (EARI). The averages for different data sets would reduce

the data uncertainties and noises, which is important for signal detection. A similar domain was also used to measure East African short rains in previous studies [e.g., *Behera et al.*, 2005; *Manatsa and Behera*, 2013; *Gitau et al.*, 2015; *Philippon et al.*, 2015]. In particular, the precipitation within the domain exhibited temporal-spatial coherence. October EARI exhibited a variance of 1.97 $(mm\ d^{-1})^2$, which is the largest of all of the months. Approximately 85% of the total variance of EARI originated from the interannual timescale variations.

2.2. Methodology

We high-pass filtered all the time series by using a Butterworth filter to focus on the interannual variations in the variables of interest, and only the components with time periods that were shorter than 10 years were retained and employed in the following analysis.

Furthermore, we excluded the influence of the ENSO and IOD to isolate the impact of the AO on tropical climates. We removed the ENSO and IOD's variance in the variables of interest through linear regression analysis. The ENSO and IOD have a phase-locking feature with a mature peak in boreal winter and autumn, respectively, and their climate influences may be multiseasonal, so we consider the simultaneous Pacific and Indian Ocean SSTs and their preceding peak conditions. Given a specific time series (y), we used a simple equation to estimate the variance that was linearly related to the ENSO and IOD:

$$\hat{y} = b_1 E_1 + b_2 E_2 + b_3 I_1 + b_4 I_2 \qquad (1)$$

where $b_1, b_2, b_3,$ and b_4 are regression coefficients; E_1 and I_1 are the Niño 3.4 SST and IOD in the simultaneous autumn; E_2 is Niño 3.4 SST during the preceding winter; and I_2 is the IOD during the preceding autumn. $\hat{y}$ was estimated by using the least squares technique and was then subtracted from the climate time series. The residuals (i.e., $y - \hat{y}$) were regarded as "ENSO- and IOD-free" parts and were subjected to the following analysis. Composite analysis was also employed and compared with the regression analysis.

3. East African Precipitation Anomalies

3.1. Precipitation Anomalies

After high-pass filtering the precipitation time series and linearly removing the ENSO and IOD variance, we computed the anomalies of the monthly precipitation rates that corresponded to the JFM AO index. Considering the dramatic month-to-month changes in the background atmospheric circulations during early short rain seasons [e.g., *Mutai and Ward*, 2000], we investigated anomalous precipitation for each of the months of September, October, and November. The results are shown in Figure 2. None of the data sets showed significant anomalies over East Africa or the neighboring Indian Ocean in November. In September, significant anomalies below 0.4 mm d^{-1} appeared in a few scattered grids over the western Indian Ocean, especially in the GPCP and CMAP data sets. By contrast, the precipitation anomalies in October displayed an evident pattern, with notable spatial coherence among all the data sets. The salient feature was the significant positive autumn precipitation anomalies over the equatorial East Africa under a positive winter AO phase. The location and extent of the anomalies were generally similar among the four data sets, approximately covering a key region between 5°S–5°N and east of 35°E, where the maxima were approximately 0.4–0.8 mm d^{-1} in association with one unit of the JFM AO index. We further examined the temporal features of this precipitation. As shown in Figure 3, the October EARI (as averaged over 5°N–5°S and 35°–45°E) showed notable in-phase year-to-year variations with the JFM AO index. The precipitation maxima of 1982, 1997, 2009, and 2011 cooccurred with strong positive AOs, whereas the JFM AO indices were relatively low in the anomalously dry years of 1996, 2010, and 2013. Indeed, the Pearson correlation between the October EARI and the JFM AO was +0.51. Their correlation still remained +0.46 after the IOD and Niño3.4 SST signals were removed. Both values were statistically significant at the 0.05 level. When the apparent outstanding value of 1997 was excluded, the EARI was still significantly correlated with the JFM AO (+0.44). In addition, we analyzed the precipitation anomalies for the short rain season. The JFM AO was correlated with September–November EARI at +0.32. For October–November the correlation was +0.30. Although these values were statistically significant at the 0.1 level, we found it was hard to make a physical explanation. In fact, September and November EARI showed no evident anomalies, and their correlations were only +0.18 and +0.07, respectively. This is clearly shown in Figure 2. Thus, the majority of the AO-related seasonal precipitation variance was contributed by the October anomalies.
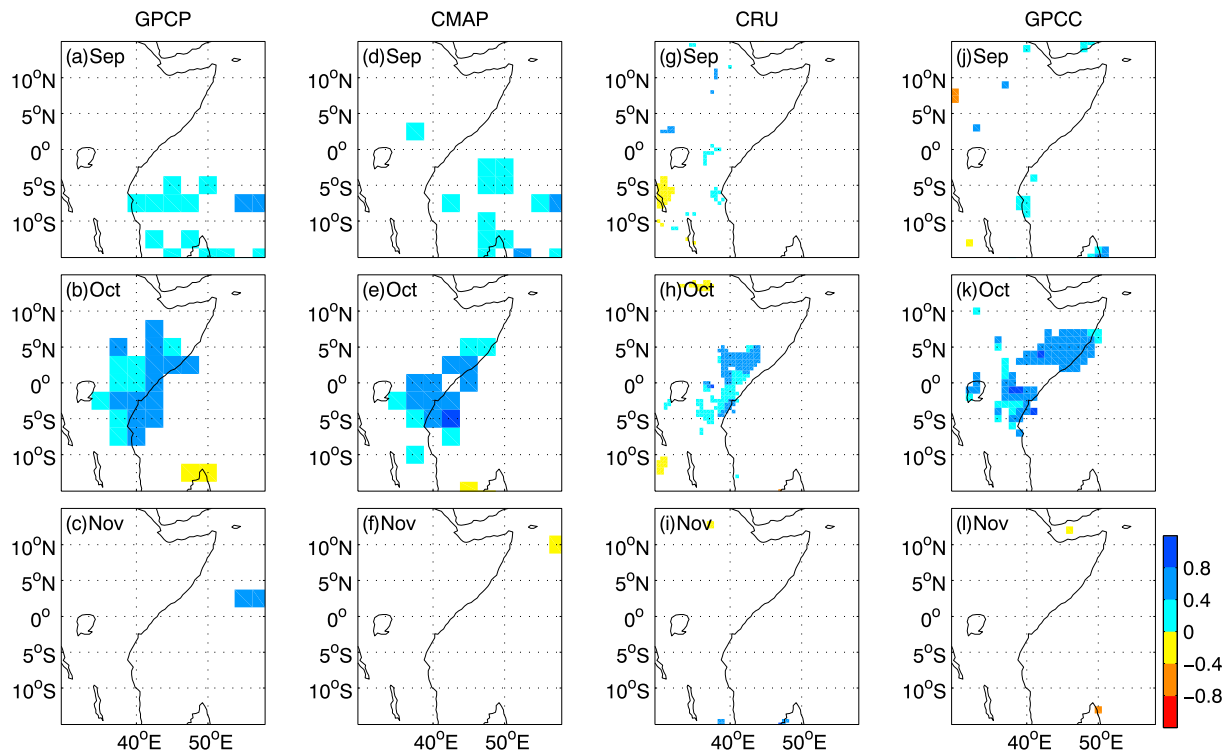
Figure 2. Interannual precipitation anomalies from September to November in association with the JFM AO index. All of GPCP, CMAP, CRU, and GPCC are analyzed using the same period of 1979–2014. Only values significant above the 0.05 level are shown. Unit: mm d^{-1}.

It should be pointed out that the regression analysis was performed based on the residuals after high-pass filtering and removing the IOD and ENSO's variance. A disadvantage of this method is the potential negligence of possible nonlinearity in the relationship. For further clarification, we additionally examined the precipitation composites based on the JFM AO index. Because the CRU and GPCC data sets are available only for land areas, we utilized the GPCP and CMAP data sets to calculate the precipitation anomalies in a broader area that extended from East Africa to the neighboring western tropical Indian Ocean. We compared the October precipitation differences between the positive JFM AO years and the negative AO years. The period of 1979–2014 exhibited four strong positive AO years (1989, 1990, 1993, and 2002) when the JFM AO indices were larger than 1 standard deviation (i.e., AO > 1σ) and six strong negative AO years (1979, 1980, 1985, 1987, 2010, and 2013), for which the anomalies were smaller than −1σ. The autumn IODs for the years 2002 and 2010 were also intense (anomalies beyond ±1σ). Therefore, these 2 years were excluded from the composites to reduce the influence of the IOD. Finally, we computed the precipitation means for three positive AO years
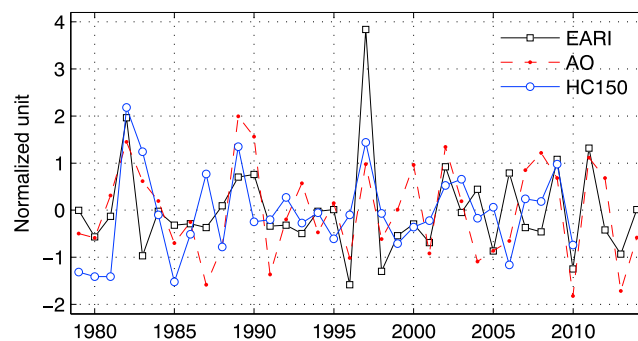

Figure 3. Time series of the JFM AO index, October East African rainfall index (EARI), and the ocean heat content in the uppermost 150 m (HC150) averaged over 40°–60°E and 5°–10°S. All time series are normalized with respect to the whole data period to facilitate comparison.
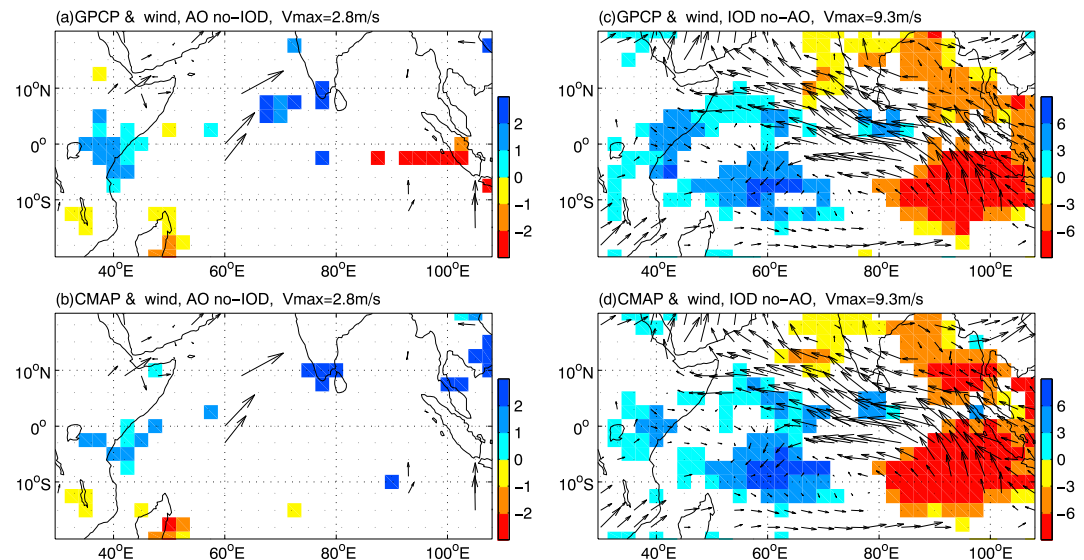
Figure 4. Composites of precipitation in October based on the (a, b) JFM AO indices and (c, d) the autumn IOD indices. Precipitation anomalies are shown in colors with unit of mm d^{-1}. Horizontal wind vectors at 850 hPa are superimposed. Only values significant at the 0.1 level are plotted.

(i.e., 1989, 1990, and 1993), five negative AO years (i.e., 1979, 1980, 1985, 1987, and 2013), and then their differences (the positive minus the negative). The statistical significance levels of the differences were estimated by using a two-tailed t test.

Figure 4 shows the results of the composites. Both the GPCP and CMAP data sets displayed significant positive anomalies in equatorial East Africa and the nearby Indian Ocean. A couple of grids of positive values were scattered near southern India, but the signals in these grids did not seem to be stable between the GPCP and CMAP data sets. The spatial feature over East Africa agreed well with the regression analysis. It is obvious that the AO-related anomalous precipitation pattern was markedly different from the IOD-related pattern. For comparison, we generated IOD composites. The period 1979–2014 exhibited six strong positive IOD events with autumn IODs > 1σ (i.e., 1982, 1994, 1997, 2002, 2006, and 2012) and four strong negative event with autumn IODs < −1σ (i.e., 1996, 1998, 2005, and 2010). The concurrent intense JFM AO events in 2002 and 2010 (both beyond ±1σ) were excluded. Therefore, five positive IOD cases (1982, 1994, 1997, 2006, and 2012) and three negative IOD cases (1996, 1998, and 2005) were employed in the IOD composites. As shown in Figure 4, the IOD-related precipitation featured a west-east-oriented dipole with drier conditions in the eastern Indian Ocean and wetter conditions in the central and western Indian Ocean, which is a similar pattern to those reported in previous studies [*Saji et al.*, 1999; *Webster et al.*, 1999]. The IOD-related positive anomalies in the East African coastal regions were apparently collocated with the AO-related anomalies, but the former had much larger magnitudes. For example, the maximum values in equatorial East Africa were approximately 3–6 mm d^{-1}, whereas the AO-related maxima were 1–2 mm d^{-1}. More importantly, the anomalous atmospheric circulation was completely different. We calculated the composites for 850 hPa horizontal winds and superimposed these values onto the precipitation anomalies. As shown in Figures 4a and 4b, no meaningful wind anomalies existed for the AO-related composites, whereas IOD-related atmospheric circulation was dominated by significantly strong easterly winds at a basin scale. This result suggests that the IOD-related precipitation was tightly coupled with basin-scale circulation, whereas the AO-related precipitation was unlikely related to large-scale circulation. Generally, the composites displayed a highly similar feature to the regression analysis in equatorial East Africa, likely reflecting the winter AO-early short rain linkage. The difference in precipitation and circulation between the AO and IOD composites probably implies a different mechanism that involves the AO-short rain relationship. It should be pointed out that both the linear regression and composite analysis cannot perfectly remove the IOD and ENSO variance in a coupled climate system. Meanwhile, the physical processes linking the JFM AO and the western Indian Ocean thermal condition/short rains were found different from that of IOD/ENSO (see also *Gong et al.* [2016]). A different mechanism likely provided confidence of a robust and independent influence of the JFM AO.
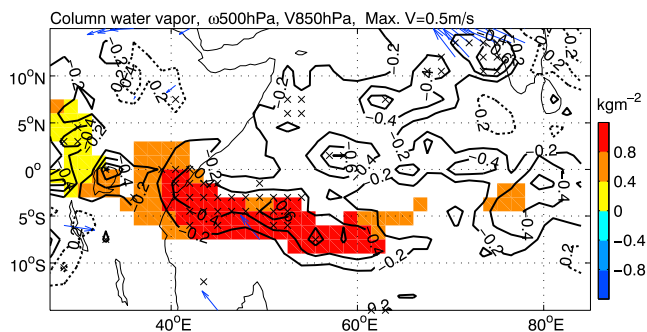
Column water vapor, ω500hPa, V850hPa, Max. V=0.5m/s

Figure 5. Anomalies of the total column water vapor (colors, kg m^{-2}), 850 hPa horizontal winds (vectors, m s^{-1}), and 500 hPa vertical velocity (contours, solid line indicates ascending motion and the dashed line indicates descending motion, unit: 10^{-2} Pa s^{-1}) in association with the JFM AO index. Only significant (at the 0.05 level) water vapor and 850 hPa winds are shown. Significant 500 hPa vertical motion is indicated by cross symbols.

3.2. Atmospheric Circulation and Humidity

The previous section demonstrated that equatorial East Africa tended to gain more precipitation in October, corresponding to a larger JFM AO index. Anomalous precipitation could directly result from anomalous atmospheric circulation, anomalous moisture, or both. Here we investigated the changes in both the atmospheric circulation and troposphere humidity. The horizontal winds at 850 hPa, the vertical motion at 500 hPa, and the total column water vapor were analyzed as with the precipitation analysis (i.e., these variables were high-pass filtered first, the IOD and ENSO's variance was linearly removed, and finally, the variables were regressed upon the JFM AO index). Their regression coefficients are shown in Figure 5. The dominant feature was the significant increase in the water vapor in the western Indian Ocean between approximately 0° and 10°S. The maxima of >0.8 kg m^{-2} extended from approximately 65°E to the coast. The values in the majority of equatorial East Africa east of 35°E were between 0.4 and 0.8 kg m^{-2}. Even the inland area west of 30°E between 0° and 5°N exhibited positive anomalies <0.4 kg m^{-2}. At 850 hPa, no significant horizontal wind anomalies existed, which is consistent with the composite analysis results. Clearly, anomalous water vapor was unlikely to have been brought by large-scale anomalous atmospheric circulation through horizontal transport or convergence. The AO-related vertical air motion at 500 hPa indicated significant ascending along approximately 5°S west of 55°E. The locations of this strong ascending and the anomalous water vapor in the western Indian Ocean were almost identical, which suggests that in situ evaporation and convection played a major role.
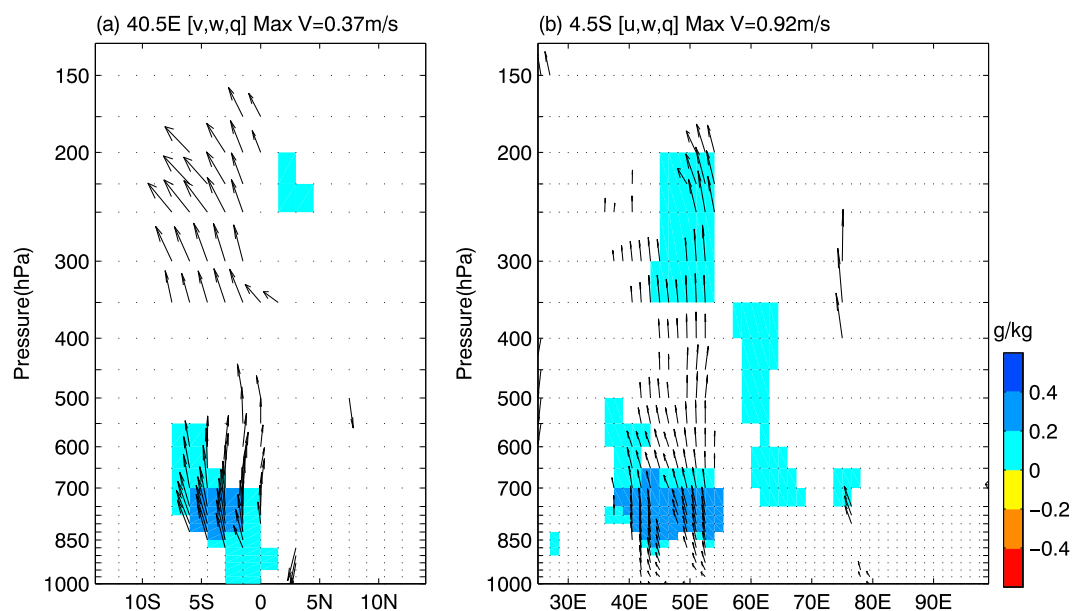

(a) 40.5E [v,w,q] Max V=0.37m/s   (b) 4.5S [u,w,q] Max V=0.92m/s

Figure 6. Anomalies of wind velocity and specific humidity (a) in the latitude-pressure section along 40.5°E and (b) in the longitude-pressure section along 4.5°S. Only values significant at the 0.05 level are shown.

These results are further supported by the anomalous vertical profiles of the vertical motion and humidity. Figure 6 shows the latitude-height section of the specific humidity and the meridional and vertical velocity along 40.5°E. An anomalous specific humidity was located below 650 hPa, with a maximum of 0.2–0.4 g kg^{-1} between 850 and 700 hPa that was centered at 5°S. Significant upward motion was located between 0° and 7°S and extended from 850 hPa to 250 hPa with a maximum of 0.37 m s^{-1}. The longitude-height section along 4.5°S revealed that the positive humidity anomalies spread from the lower troposphere upward to 200 hPa in association with strong ascending between 40° and 50°E. Smaller positive humidity anomalies could also be found to the east at approximately 60°–75°E. The background circulation in October was the overwhelming southeasterly, which transported the anomalous moisture horizontally from the western Indian Ocean westward into the East African continent [e.g., *Chan et al.*, 2008; *Mutai and Ward*, 2000]. Therefore, the local/regional moisture transport and active convection created above average precipitation over equatorial East Africa. In addition, some synoptic systems that originated in the western Indian Ocean may penetrate into the coastal continent in the presence of strong southeastern winds and produce precipitation along their development over the continent [*Mutai and Ward*, 2000].

4. Possible Mechanisms

4.1. Anomalous Upper Ocean Heat Content

One question is how the JFM AO enhances the atmospheric humidity and convection over the western Indian Ocean in October. Usually, a warmer SST tends to enhance evaporation and convection. We calculated the changes in the SST in October in association with the JFM AO index and found that only moderate anomalies existed over the western Indian Ocean, which were not statistically significant (figure not shown). We argue that this result was likely related to local air-sea coupling and feedbacks [e.g., *Xie et al.*, 2002; *Chowdary et al.*, 2009; *Du et al.*, 2009; *Webber et al.*, 2010, 2012]. Instead of the SST, we analyzed the upper ocean heat content in October, which has important climate consequences in terms of heat storage and release [*Annamalai et al.*, 2005; *Xie et al.*, 2009]. Considering the climate depth of the thermocline, we calculated the heat content for the uppermost 150 m (HC150). Just as in the precipitation analysis, we first high-pass filtered the HC150 time series, then linearly removed the IOD and ENSO signals, and finally computed the regression coefficient upon the JFM AO index. The results are shown in Figure 7. The salient feature was the belt of evident positive anomalies near the western coast between 5° and 10°S and west of 60°E, where the maximum was approximately 2–3 × 10^8 J m^{-2}. Interestingly, the location and extent of the anomalous HC150 coincided with the moisture and vertical motion anomalies (compare Figures 5 and 7). We further examined the temporal variations in the regional mean HC150 (averaged over 40°–60°E and 5°–10°S). As demonstrated in Figure 3, the October ocean heat content generally varied in phase with the JFM AO. Two time series were correlated at +0.50, which was significant at the 0.05 level (Table 1).

Meanwhile, the simultaneous correlation between the October HC150 and EARI was +0.53. The robust HC150-EARI relationship was supported by the corresponding anomalies in the atmospheric moisture and precipitation. After linearly removing the IOD and ENSO's variance, we computed the regression of the GPCP rainfall, the total column water vapor, and the 850hPa horizontal winds upon the regional mean HC150. In association with larger upper ocean heat content, the precipitation over the East African continents was significantly enhanced, with a maximum of approximately 1–2 mm d^{-1}. The analysis for the CMAP data sets yielded a similar pattern (figure not shown). The simultaneous change in the column water vapor featured a moist center in the western Indian Ocean, where the anomalies were above 1 kg m^{-2}. The extent of this significant amount of water vapor covered a larger area north of the location of the anomalous HC150 (cf. Figures 7 and 8). This result was likely caused by the background atmospheric circulation, which helped spread the anomalous moisture westward and northward in the tropical western Indian Ocean. This pattern apparently differed from that of the IOD-related anomalies. For comparison, we replotted the HC150-related changes but did not remove the IOD and ENSO's variance. The atmospheric moisture was clearly dominated by a west-east dipole. The southeastern Indian Ocean exhibited negative anomalies, whereas positive anomalies over the western Indian Ocean west of 75°E were evidently larger than those without the IOD and ENSO's variance. In addition, the lower troposphere winds were different. In Figure 8b, the salient feature of the 850 hPa winds was a basin-wide C-type anomaly. Without the IOD and ENSO's variance, only anomalous easterlies occurred along the equator east of 70°E. These easterlies were likely related to precipitation diabatic heating over the western Indian Ocean [e.g., *Webber et al.*, 2010]. However, these anomalous winds were relatively weak, with means of 1.1 m s^{-1} along the equator between 70° and 100°E (Figure 8a), whereas the winds at the same longitudes
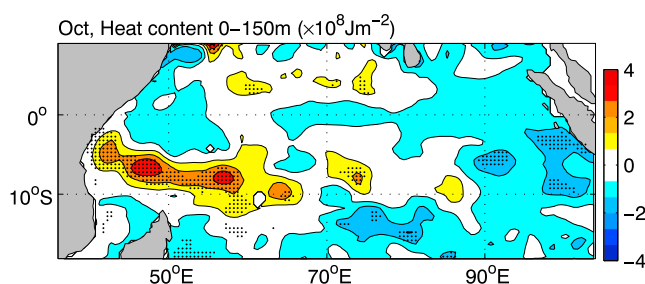
Figure 7. October heat content anomalies in association with the JFM AO index. Stipples denote values significant at the 0.05 level.

shown in Figure 8b were approximately 2 times stronger (2.4 m s^{-1}). Generally, the evident linkage between the JFM AO and October HC150 likely suggests that the upper ocean heat content in the western Indian Ocean played a key role in "storing" the winter AO signals and further affected East African early short rains.

4.2. Oceanic Rossby Wave Induced by AO Forcing

Why does anomalous heat content exist in the western Indian Ocean in October? We analyzed the vertical temperature profiles by using SODA data to more clearly show changes in the heat content. The longitude-depth section from the western Indian Ocean to the east averaged between 5° and 10°S are plotted in Figure 9. Anomalous warmer temperatures for the positive JFM AO cases appeared in the upper layers, with a maximum >0.6°C near the 20°C isotherm to the west of 60°E in October. After October, the temperature anomalies between 40° and 60°E rapidly weakened and disappeared by December. Interestingly, strong subsurface warming in the western Indian Ocean actually appeared during the late summer. In August, an anomalous warming of >0.3°C spanned from 40 m to approximately 160 m. The strongest warming was located around the thermocline. We plotted the JFM AO-related temperature vertical profiles back to January and the preceding autumn to show where and when this anomalous subsurface warming originated. Results showed that this subsurface warming first formed during the boreal winter in the middle of the Indian Ocean and then propagated westward. As clearly demonstrated in Figure 9, the center of the subsurface warming in February was between approximately 65° and 75°E. Later, this center moved to 60°–65°E and 55°–60°E in April and June, respectively. No such warming was present before January. Evidently, this subsurface warming resulted from a Rossby wave and its westward propagation along the thermocline, which formed in the central tropical Indian Ocean during boreal winter.

Oceanic dynamics are recognized as the primary processes that sustain and propagate subsurface temperature variations. Oceanic Rossby waves are important in forming tropical Indian Ocean variability at time scales ranging from intraseasonal to interannual (*Huang and Kinter* [2002], *Izumo et al.* [2008], *Gnanaseelan and Vaid* [2010], *Chakravorty et al.* [2014], among others). One important origin is the anomalous wind stress, which dynamically causes regional Ekman pumping and further generates a forced Rossby wave. We examined simultaneous changes in near-surface winds, the thermocline depth, and the sea surface height to determine whether winter AO-related atmospheric circulation generates oceanic Rossby waves in the Indian Ocean. As shown in Figure 10, anomalous winds crossed the equator with a C-type pattern in the central tropical

Table 1. Correlations Among October East African Precipitation (EARI), the Upper Ocean Heat Content in the Top 150 m (HC150), and the January–February–March AO Index[a]

	AO(JFM)	HC150(Oct.)	EARI(Oct.)
AO(JFM)	/	+0.49[b]	+0.51[b]
HC150(Oct.)	(+0.50[b])	/	+0.45[b]
EARI(Oct.)	(+0.46[b])	(+0.53[b])	/

[a]In parentheses are correlations after removing ENSO and IOD variance. The HC150 is averaged over 40°–60°E and 5°–10°S.
[b]Significant at the 0.05 level.

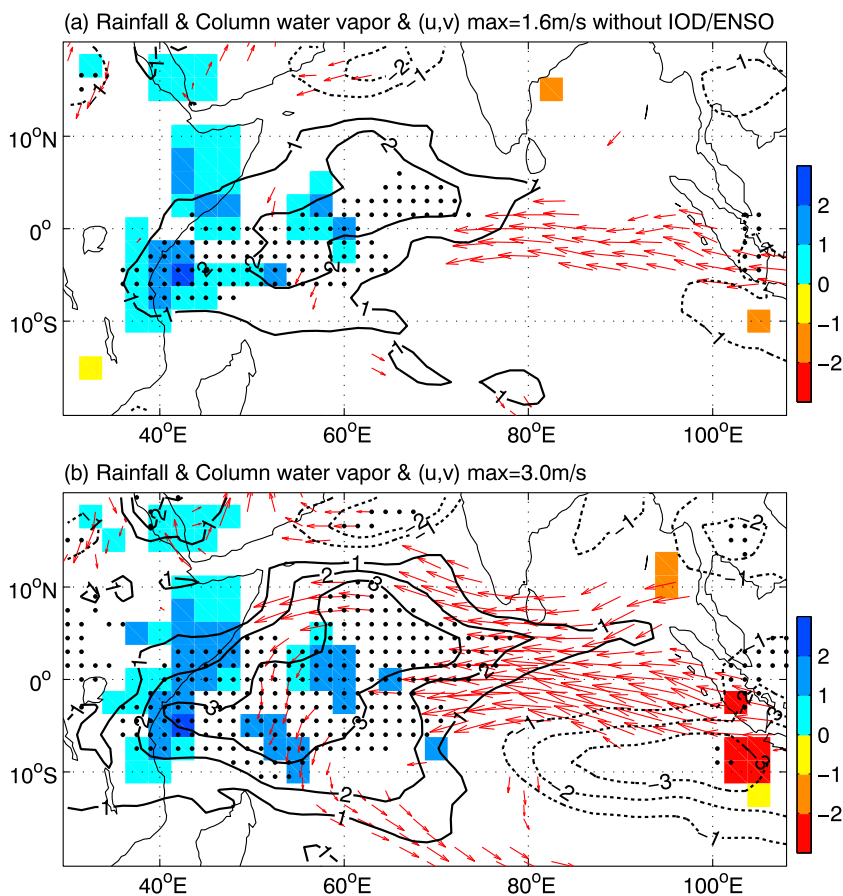**Figure 8.** Anomalous GPCP rainfall (colors, mm d^{-1}), total column water vapor (contours, kg m^{-2}), and 850 hPa horizontal winds (vectors, m s^{-1}) in association with the regional mean upper ocean heat content over 40°–60°E and 5°–10°S. Only significant (at the 0.05 level) GPCP and winds are plotted. Significant total column water vapor is denoted by stipple. (a) The IOD and ENSO variance have been removed and (b) IOD and ENSO variance have not been removed.

Indian Ocean between 60° and 70°E, in association with a larger JFM AO index. The significant crossing equatorial air flow in the same location existed from surface to 500 hPa. *Gong et al.* [2014] reported that atmospheric Rossby waves that are guided by westerlies during positive AO winters tend to trigger persistent positive geopotential heights in the upper troposphere over approximately 20°–30°N and 55°–70°E. Anomalous downward air motions strengthened the air pressure in the middle to lower troposphere. Thus, the enhanced Arabian High brought anomalous northern winds over the northern Indian Ocean, in turn creating anomalous cross-equatorial air flows in the central tropical Indian Ocean. Naturally, this C-type wind stress induced downwelling Ekman pumping. The thermocline around 60°–75°E and 5°–10°S significantly deepened by >4 m. Correspondingly, the sea surface height was approximately 2 cm above normal. A similar pattern of circulation and thermocline changes that corresponded to the winter AO was also reported in observations and simulations [e.g., *Gong et al.*, 2014, 2016]. These results are robust signals of downwelling Rossby waves. The traveling speed of the Rossby wave as estimated from Figure 9 was approximately 14 cm s^{-1}, which is a typical baroclinic Rossby wave speed [*Chelton et al.*, 1998; *Vasala*, 2008]. In addition to the subsurface positive temperature anomalies, the arrival of Rossby wave in the western Indian Ocean also caused the significant warming in SSTs by approximate 0.2°–0.3°C in July–August [see *Gong et al.*, 2016, Figure 1]. Numerical experiments showed that without the arrival of the downwelling Rossby wave, the western Indian Ocean SSTs cooled significantly [*Tozuka et al.*, 2014]. Another simulation study showed that the upwelling Rossby wave generated by wind stress over the Seychelles Dome in November and December resulted in SST cooling during the subsequent spring and early summer over the western Indian Ocean [*Manola et al.*, 2015]. It should be pointed
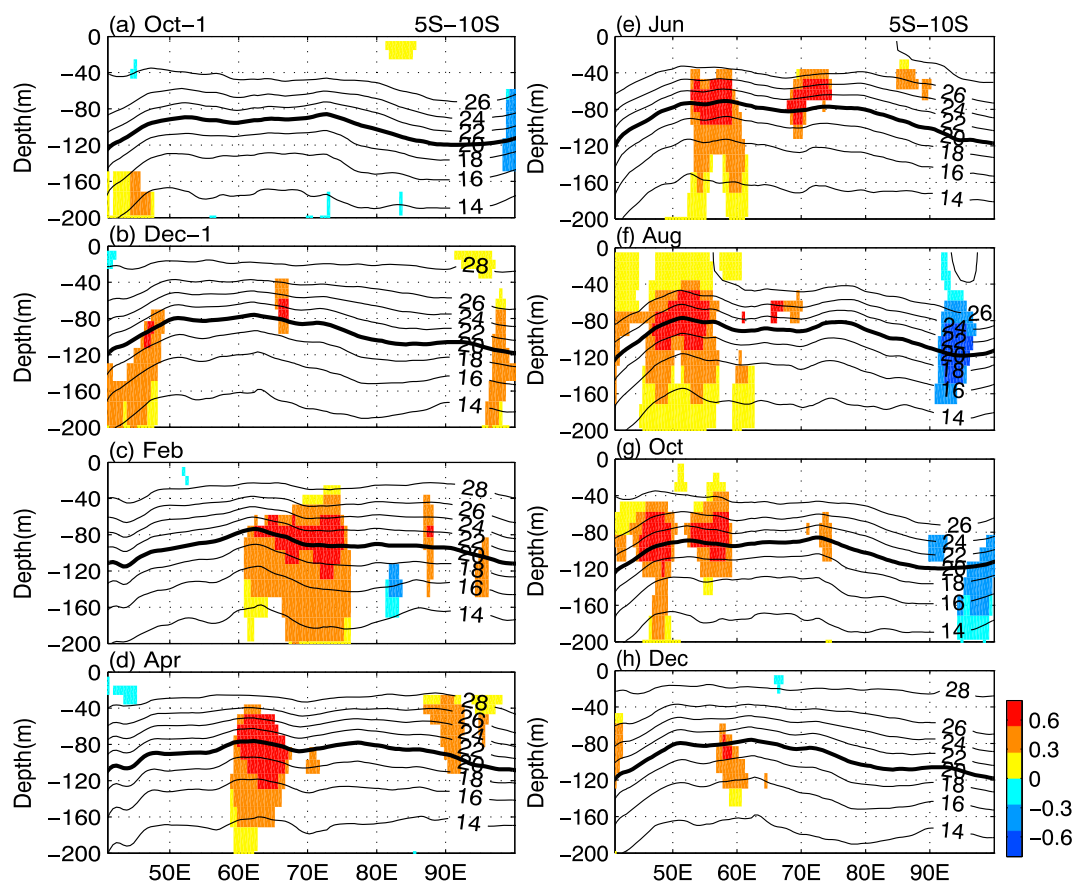
Figure 9. Temperature anomalies averaged from 5°–10°S in association with the JFM AO index from preceding October to the concurrent December plotted for every other month (colors: °C). Contour lines are long-term mean temperature (°C), and the 20°C isotherm depth is shown in bold line. Color shadings denote significant values at the 0.05 level.

out that the SST anomalies decayed rapidly and no longer significant after August, whereas the positive upper ocean heat content anomalies persisted into September and October. In addition, the net surface heat fluxes were negative anomalies in a small region close to the coast at approximate 5°S, implying that the western Indian Ocean still released heat to the atmosphere in September–October [cf. *Gong et al.*, 2016, Figure 6]. This was consistent with the positive anomalies in HC150, the increased in situ atmospheric humidity, and the enhanced convection.
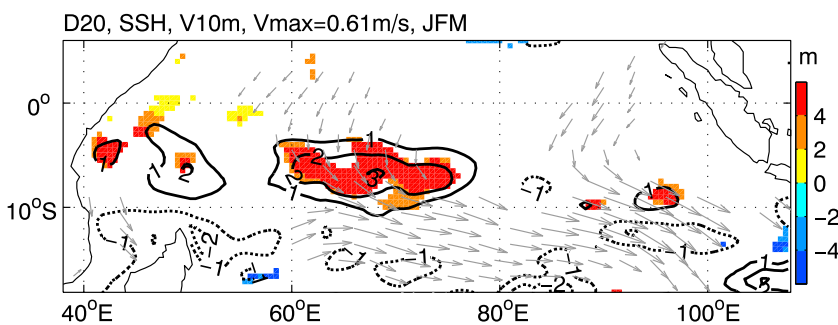

Figure 10. Anomalous 10 m winds (vectors with units of m s^{-1}), 20°C isotherm depth (D20, colors with units of m), and sea surface height (SSH, contours with units of cm) in association with the JFM AO index. Plotted D20 and winds are both significant at the 0.05 level.

5. Numerical Experiments

5.1. Numerical Experimental Design

Observation analysis demonstrated that a slowly propagating oceanic Rossby wave existed that strongly covaried with the thermocline and behaved very differently from those that are damped by air-sea interactions [e.g., *Xie et al.*, 2002]. This observation likely implies that oceanic dynamics, rather than air-sea fluxes, dominated the wave's propagation from the central Indian Ocean to the west and induced the anomalous upper ocean warming over the southwestern Indian Ocean [e.g., *Annamalai et al.*, 2005; *Gong et al.*, 2016]. We performed numerical experiments by using an oceanic general circulation model of the Miami Isopycnic Coordinate Ocean Model (MICOM) [*Bleck et al.*, 1992] to clarify this issue and focus on the oceanic dynamics. The MICOM has 34 isopycnic layers in the vertical direction and a nonisopycnic surface mixed layer on top. Its horizontal resolution is 2.4° along the equator, and the meridional resolution near the equator is 0.8° to better resolve equatorial confined dynamics. We first performed spin-up integration to prepare for the numerical experiments. In this step, the MICOM was forced by the daily NCEP-NCAR (National Centers for Environmental Prediction-National Center for Atmospheric Research) atmosphere from 1 January 1948 to 31 December 2009. The same atmosphere-forcing integration was repeated 4 times without interruption. The last 61 years (i.e., 1948–2009) were retained to provide the initial conditions for the control runs. We selected all the grids where the near surface winds were significantly correlated to the JFM AO index in the domain of 40°–100°E and 20°S–20°N to highlight the wind stress over the Indian Ocean (see Figure 10). We multiplied these wind vectors by the regional mean wind stress climate (0.04 N m^{-2}) to enhance the AO-related signals. In other words, the amplified wind stresses in the anomalous forcing field were assigned in proportion to their AO-related wind anomalies only at these significant grids, whereas the values for the nonsignificant grids and those outside the domain were all zero. We should point out that on the boundary between enhanced and normal grid points, there would be spurious wind shear though its scale might be small. Its possible influence on the simulations needs a greater refinement analysis.

When designing the numerical experiments, two important issues had been considered. First, in order to simulate the AO's oceanic impact, the numerical experiments should start from normal AO conditions. We examined the original unfiltered JFM AO time series and found that the year of 1991 had the smallest magnitude (only −0.23) in all non-IOD/ENSO years. Therefore, the year of 1991 was selected as the normal AO case for numerical experiments. Second, the possible influence of other climate modes should be tested. The most important mode in Indian Ocean climate variability is the IOD. In all strong IOD cases with their magnitudes exceeding 1σ, the year 1994 had the smallest magnitude for JFM AO (+0.24). Thus, the year 1994 was selected for numerical experiments as a normal-AO plus positive-IOD case.

Then, we performed control runs for 1991 with an initial condition from the spin-up ocean on 1 January 1991. The NCEP-NCAR atmospheres from 1 January to 31 December 1991 were imposed onto the MICOM. This process was repeated 50 times without interruption. The means of these control runs should mimic the observational ocean climate. The first sensitivity run for 1991 used the same initial condition as the first control run. The initial conditions from the second to the fiftieth sensitivity runs were taken from the first day in each of the parallel control runs. Thus, each pair of control and sensitivity runs began from exactly the same conditions. The AO-related anomalous forcing field during these 50 sensitivity runs was superimposed onto the NCEP-NCAR atmospheres from 1 January to 31 March and then removed until 31 December. The control and sensitivity runs for the year 1994 were conducted in the same way. In total, we obtained 50 ensembles for each year. The means of the 50 ensembles were computed. Theoretically, differences between the sensitivity and control runs were caused by the AO-related forcing over the Indian Ocean in January–March. And by comparing the results between 1991 and 1994, we might get an idea whether the IOD impacted the AO's influence on the western Indian Ocean thermal condition and short rains.

5.2. Simulated Oceanic Changes

We first examined whether the westward propagation of the subsurface temperature anomalies was reproduced by the AO-forcing simulations. The differences in the mean water temperature averaged from 5° to 10°S were computed from January to December. Then, the depth-longitude section was plotted in Figure 11. Here we show the results for every other month to facilitate comparisons with the observations. February exhibited two subsurface warming centers for both years. One center was located in the eastern Indian Ocean near 90°E, with a maximum >0.4°C between 80 and 120 m, and the other center was located in the central Indian Ocean near 70°E, with >0.3°C anomalies at 80–100 m depth. Interestingly, the center in the central Indian Ocean exhibited clear westward propagation. In April, the center moved to 65°–70°E, where strong
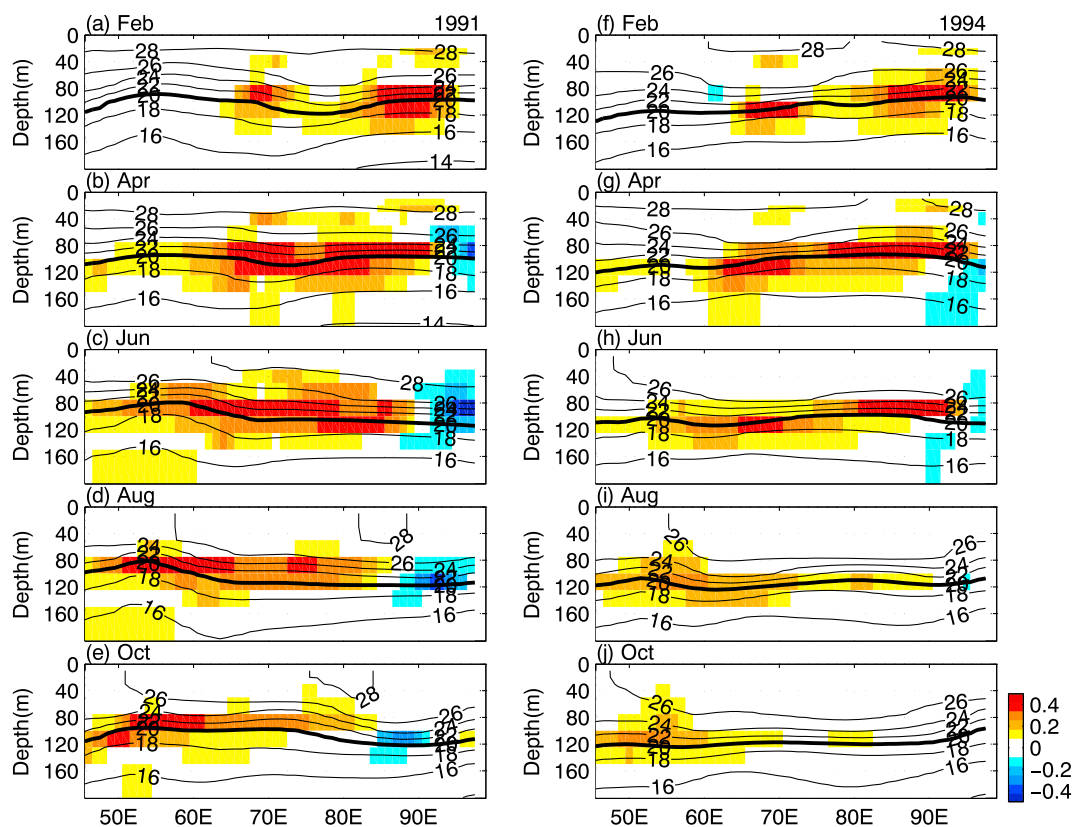
Figure 11. Simulated temperature changes averaged from 5°–10°S in response to the JFM AO wind stress forcing for simulations of (a–e) year 1991, and (f–j) year 1994. The long-term means of the temperature are superimposed as contours, and the 20°C isotherms are shown in thick lines. Shown as the difference of the sensitivity minus the control runs based on 50 ensembles. Unit: °C.

subsurface warming occurred at 80–120 m depth. Its location changed to 60°–65°E and 50°–60°E in June and August, respectively. The winter warming in the eastern Indian Ocean was likely caused by the model bias of the thermocline. The shallowest thermocline in the observations was located in the western Indian Ocean near 60°E (Figure 9); by contrast, the thermocline depth to the east was 10–20 m deeper. The model climate had two shallow centers, one at approximately 55°E and the other at 90°E (Figure 11). An unreal shallower

Figure 12. Simulated changes of the ocean heat content in the upper most 150 m in October for the years (a) 1991 and (b) 1994. Shown as the difference of the sensitivity minus the control runs based on 50 ensembles.

thermocline in the eastern Indian Ocean implied a larger sensitivity to the surface wind stress and probably produced amplified subsurface warming. In addition, by comparing simulations for 1991 and 1994, we found that the subsurface warming in 1994 was somewhat smaller than that in 1991.
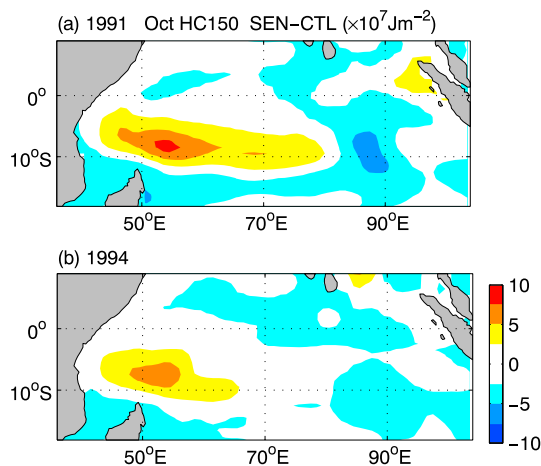
The striking feature of the AO-related subsurface changes in the observations was that the largest anomaly traveled from the central Indian Ocean in the winter to the west in the summer along the thermocline (Figure 9). This dominant oceanic dynamics was adequately reproduced in the numerical experiments, and the positive subsurface anomalies remained in the western Indian Ocean west of 60°E until October (Figure 11). Correspondingly, the upper ocean heat content over the western Indian Ocean increased in October. As displayed in Figure 12a,
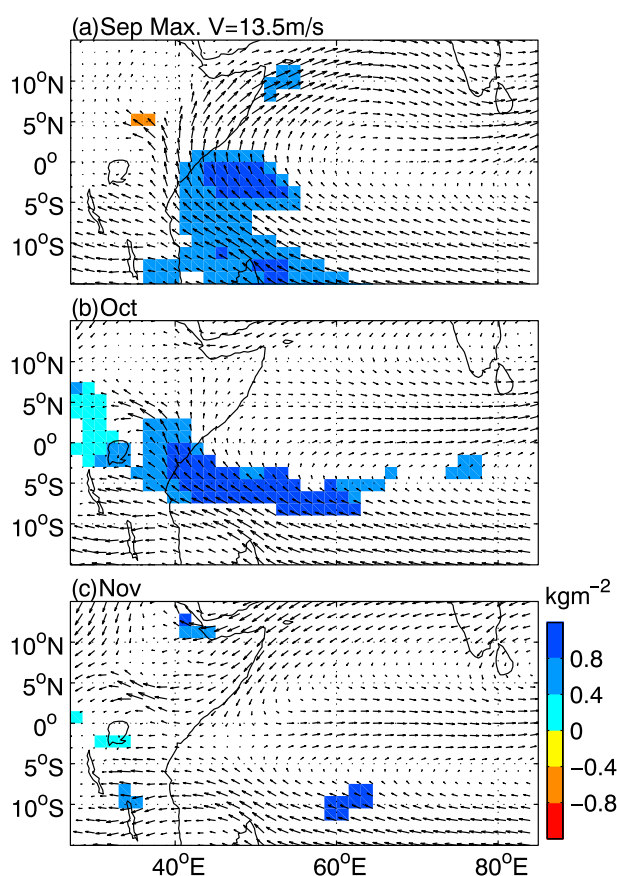
Figure 13. Anomalies of the total column water vapor (significant at the 0.05 level) in association with the JFM AO index. The long-term mean horizontal winds at 850 hPa level are superimposed.

evident positive heat content anomalies appeared from 40° to 80°E between approximately 0° and 10°S for simulations of 1991. An anomalous center with a value $>5 \times 10^7$ J m^{-2} was located around 50°–60°E and 5°–10°S. This extent in the simulation agreed with that from the observations (cf. Figures 7 and 12). The simulations for 1994 revealed a similar pattern of warming in the upper ocean over the western Indian Ocean, but the magnitude was slightly smaller than the year 1991 (Figure 12b). Generally, the observed and simulated western Indian Ocean subsurface temperature anomalies that resulted from an AO-related Rossby wave were consistent with the theoretical baroclinic Rossby wave model and ocean general circulation model simulations [e.g., *Zhuang et al.*, 2013; *Tozuka et al.*, 2014; *Manola et al.*, 2015]. Why the warming in 1994 was smaller than in 1991 is an interesting topic. The different ocean conditions between 1991 and 1994 seemed a possible reason. For example, the thermocline in 1994 was generally deeper than in 1991 and its spatial distribution was also different. Anyway, the results for 1994 suggested that the physical processes
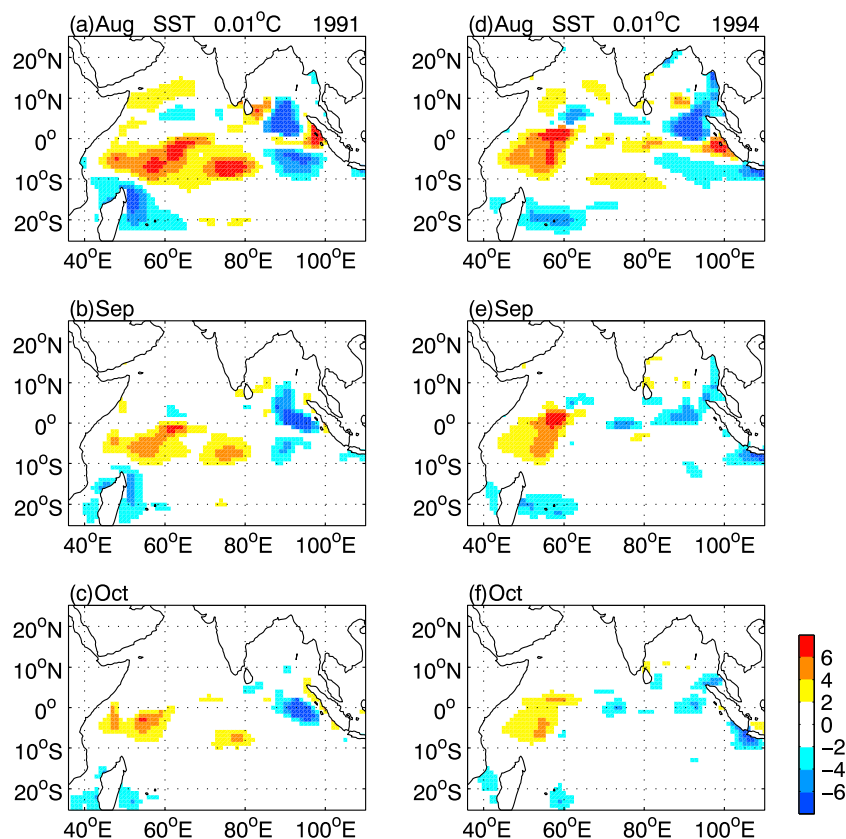
involving the JFM AO and consequent oceanic dynamics were likely robust and independent of the climate background/modes. In positive IOD years, the strong positive JFM AO would bring more short rains than non-IOD conditions.

6. Conclusions and Discussion

6.1. Conclusions

In this study, we analyzed the interannual linkage between the boreal winter AO and East African short rains. A significant in-phase covariation relationship was found between the JFM AO index and the October precipitation over equatorial East Africa. The regional mean rainfall over 5°N–5°S and 35°–45°E was correlated with the JFM AO index at +0.51; after removing the IOD and ENSO's variance, this correlation remained at +0.46. The enhanced precipitation was apparently related to the regional moisture and convection, which were favored by positive upper ocean heat content anomalies in the neighboring western Indian Ocean.

A mechanism that links the winter AO and early short rains is suggested. The JFM AO-related atmospheric circulation was characterized by a simultaneous enhanced cross-equatorial air flow in the central Indian Ocean. This C-type wind stress anomaly induced a downwelling oceanic Rossby wave around 60°–75°E and 5°–10°S, where the thermocline significantly deepened by >4 m and the sea surface height was approximately 2 cm above normal. The subsurface temperature significantly changed, accompanying the westward propagation of the Rossby wave along the thermocline. In February, the center of the subsurface warming was located between approximately 65° and 75°E. Then, this center moved to 60°–65°E and 55°–60°E in April and June, respectively. The Rossby wave arrived at the western Indian Ocean in late summer, resulting in a significant warming of >0.6°C west of 55°E at a depth of 60–100 m. This warming remained significant through October. Afterward, the temperature anomalies between 40° and 60°E rapidly weakened and disappeared by December. The upper ocean heat content significantly increased in October by approximately

Figure 14. Simulated SST difference of sensitivity minus the control runs from August to October based on 50 ensembles for years (a–c) 1991 and (d–f) 1994.

$2-3 \times 10^8$ J m^{-2} in a region west of 60°E between 5° and 10°S, corresponding to subsurface warming. The upper ocean heat content enhanced the atmospheric moisture and convection over the western Indian Ocean, increasing the precipitation over downstream equatorial East Africa in the presence of background southeastern winds.

The role of oceanic dynamics in linking the winter AO and anomalous subsurface warming over the western Indian Ocean was tested by numerical experiments with an oceanic general circulation model. The experiments were performed with the forcing of AO-related wind stress anomalies over the Indian Ocean during the winter. The oceanic Rossby wave that was generated in the central Indian Ocean during boreal winter, its westward propagation, the associated subsurface warming, and the anomalous upper ocean heat content in October over the western Indian Ocean were all adequately reproduced.

6.2. Discussion

Two issues should be discussed. First, the subsurface warming and positive upper ocean heat content anomalies persisted for a couple of months over the western Indian Ocean, but the precipitation only significantly increased in October. Actually, the atmospheric moisture consistently increased in September (Figure 13). The precipitation over equatorial East Africa showed no evident changes in September; enhanced precipitation appeared over the neighboring ocean grids instead (Figure 2). This result was likely caused by the different settings in the background atmospheric circulation. The tropospheric circulation over East Africa dramatically changed from September to November. In September, the summer monsoonal circulation dominated the western Indian Ocean and the East Africa coastal regions, featuring strong southern winds. In November, northeastern winds prevailed north of 5°N, whereas eastern winds dominated the region south of 5°S. Strong southeastern winds that blew from the western Indian Ocean and penetrated into equatorial East Africa only appeared in October (Figure 13).

The other issue is why the AO-related subsurface warming over the western Indian Ocean persisted from late summer into autumn. In our numerical experiments, we found that the positive SST anomalies over the

western Indian Ocean were evident in October. As clearly shown in Figure 14, the maximum SST warming occurred in August and then weakened gradually to September and October. In October, the center of the positive SST anomalies was located in a region between 0°–10°S and west of 60°E and consistent with the HC150 changes. This feature was not seen in the observations. Note that our experiments were atmosphere-forcing simulations without feedbacks. Air-sea interactions likely played a role. For example, *Webber et al.* [2010, 2012] supposed that the coupling between atmospheric diabatic heating and oceanic Rossby/Kelvin waves over the western Indian Ocean helps maintain the upper ocean's thermal conditions. In addition, a stable barrier layer is suggested to have played an important role in maintaining subsurface warming on a regional/local scale. Rossby waves formed a thicker barrier layer. This thicker barrier layer would favor anomalous warming above the thermocline, which would intensify the air-sea coupling over the southwestern Indian Ocean and the precipitation. The light fresh water, in turn, stabilizes the barrier layer [*Chowdary et al.*, 2009; *Sayantani and Gnanaseelan*, 2015]. A detailed mechanism should be clarified in a future study.

References

Adler, R. F., et al. (2003), The version 2 Global Precipitation Climatology Project (GPCP) monthly precipitation analysis (1979–present), *J. Hydrometeorol.*, **4**, 1147–1167.

Annamalai, H., P. Liu, and S.-P. Xie (2005), Southwest Indian Ocean SST variability: Its local effects and remote influence on Asian monsoons, *J. Clim.*, **18**, 4150–4167.

Bahaga, T. K., G. M. Tsidu, F. Kucharski, and G. T. Diro (2015), Potential predictability of the sea-surface temperature forced equatorial East African short rains interannual variability in the 20th century, *Q. J. R. Meteorol. Soc.*, **141**, 16–26.

Behera, S. K., J. J. Luo, S. Masson, P. Delecluse, S. Gualdi, A. Navarra, and T. Yagamata (2005), Paramount impact of the Indian Ocean dipole on the East African short rains: A CGCM study, *J. Clim.*, **18**, 4514–4530.

Black, E., J. Slingo, and K. R. Sperber (2003), An observational study of the relationship between excessively strong short rains in coast East Africa and Indian Ocean SST, *Mon. Weather Rev.*, **131**, 74–93.

Bleck, R., C. Rooth, D. Hu, and L. T. Smith (1992), Salinity-driven thermocline transients in a wind-and thermohaline-forced isopycnic coordinate model of the North Atlantic, *J. Phys. Oceanogr.*, **22**, 1486–1505.

Branstator, G. (2002), Circumglobal teleconnections, the jetstream waveguide, and the North Atlantic Oscillation, *J. Clim.*, **15**, 1893–1910.

Carton, J. A., and B. S. Giese (2008), A reanalysis of ocean climate using Simple Ocean Data Assimilation (SODA), *Mon. Weather Rev.*, **136**, 2999–3017.

Chakravorty, S., C. Gnanaseelan, J. S. Chowdary, and J.-J. Luo (2014), Relative role of El Niño and IOD forcing on the southern tropical Indian Ocean Rossby waves, *J. Geophys. Res. Oceans*, **119**, 5105–5122, doi:10.1002/2013JC009713.

Chan, R. Y., M. Vuille, D. R. Hardy, and R. S. Bradley (2008), Intraseasonal precipitation variability on Kilimanjaro and the East Africa region and its relationship to the large-scale circulation, *Theor. Appl. Climatol.*, **93**, 149–165.

Chelton, D. B., R. A. deSzoeke, M. G. Schlax, K. El Naggar, and N. Siwertz (1998), Geographical variability of the first baroclinic Rossby radius of deformation, *J. Phys. Oceanogr.*, **28**, 433–460.

Chowdary, J. S., C. Gnanaseelan, and S. P. Xie (2009), Westward propagation of barrier layer formation in the 2006–07 Rossby wave event over the tropical southwest Indian Ocean, *Geophys. Res. Lett.*, **36**, L04607, doi:10.1029/2008GL036642.

Clark, C. O., P. J. Webster, and J. E. Cole (2003), Interdecadal variability of the relationship between the Indian Ocean zonal mode and East African coastal rainfall anomalies, *J. Clim.*, **16**, 548–554.

Du, Y., S.-P. Xie, G. Huang, and K. Hu (2009), Role of air-sea interaction in the long persistence of El Niño induced North Indian Ocean warming, *J. Clim.*, **22**, 2023–2038.

Gitau, W., P. Camberlin, L. Ogallo, and R. Okoola (2015), Oceanic and atmospheric linkage with short rainfall season intraseasonal statistics over equatorial Eastern Africa and their predictive potential, *Int. J. Climatol.*, **35**, 2382–2399.

Gnanaseelan, C., and B. H. Vaid (2010), Interannual variability in the biannual Rossby waves in the tropical Indian Ocean and its relation to Indian Ocean dipole and El Niño forcing, *Ocean Dyn.*, **60**(1), 27–40.

Goddard, L., and N. E. Graham (1999), Importance of the Indian Ocean for simulating rainfall anomalies over eastern and southern Africa, *J. Geophys. Res.*, **104**(D16), 19,099–19,116.

Gong, D.-Y., J. Yang, S.-J. Kim, Y. Gao, D. Guo, T. Zhou, and M. Hu (2011), Spring Arctic Oscillation-East Asian summer monsoon connection through circulation changes over the western North Pacific, *Clim. Dyn.*, **37**, 2199–2216.

Gong, D.-Y., Y. Gao, D. Guo, R. Mao, J. Yang, M. Hu, and M. Gao (2014), Interannual linkage between Arctic/North Atlantic Oscillation and tropical Indian Ocean precipitation during boreal winter, *Clim. Dyn.*, **42**, 1007–1027.

Gong, D.-Y., D. Guo, Y. Gao, J. Yang, R. Mao, J. Qu, M. Gao, S. Li, and S.-J. Kim (2016), Boreal winter Arctic Oscillation as an indicator of summer SST anomalies over the western tropical Indian Ocean, *Clim. Dyn.*, doi:10.1007/s00382-016-3216-2.

Harris, I., P. D. Jones, T. J. Osborn, and D. H. Lister (2014), Updated high-resolution grids of monthly climatic observations—The CRU TS3.10 Dataset, *Int. J. Climatol.*, **34**, 623–642.

Hastenrath, S. (2000), Zonal circulations over the equatorial Indian Ocean, *J. Clim.*, **13**, 2746–2756.

Hastenrath, S. (2007), Circulation mechanisms of climate anomalies in East Africa and the equatorial Indian Ocean, *Dyn. Atmos. Oceans*, **43**, 25–35.

Hastenrath, S., A. Nicklis, and L. Greischar (1993), Atmospheric-hydrospheric mechanisms of climate anomalies in the western equatorial Indian Ocean, *J. Geophys. Res.*, **98**(C11), 20,219–20,235.

Hastenrath, S., D. Polzin, and C. Mutai (2007), Diagnosing the 2005 drought in equatorial East Africa, *J. Clim.*, **20**, 4628–4637.

Hastenrath, S., D. Polzin, and C. Mutai (2010), Diagnosing the droughts and floods in equatorial East Africa during boreal autumn 2005–08, *J. Clim.*, **23**, 813–817.

Huang, B., and J. L. Kinter III (2002), The interannual variability in the tropical Indian Ocean, *J. Geophys. Res.*, **107**(C11), 3199, doi:10.1029/2001JC001278.

Hutchinson, P. (1992), The Southern Oscillation and prediction of "Der" season rainfall in Somalia, *J. Clim.*, **5**, 525–531.

Indeje, M., F. H. M. Semazzi, and L. J. Ogallo (2000), ENSO signals in East African rainfall and their prediction potentials, *Int. J. Climatol.*, **20**, 19–46.

Izumo, T., C. B. Montégut, J.-J. Luo, S. K. Behera, S. Masson, and T. Yamagata (2008), The role of the western Arabian Sea upwelling in Indian monsoon rainfall variability, *J. Clim.*, *21*, 5603–5623.

Latif, M., D. Dommenget, M. Dima, and A. Grotzner (1999), The role of Indian Ocean sea surface temperature in forcing East African rainfall anomalies during December–January 1997/98, *J. Clim.*, *12*, 3497–3504.

Liebmann, B., I. Blad, G. N. Kiladis, L. M. V. Carvalho, G. B. Senay, D. Allured, S. Leroux, and C. Funk (2012), Seasonality of African precipitation from 1996 to 2009, *J. Clim.*, *25*, 4304–4322.

Liebmann, B., M. P. Hoerling, C. Funk, I. Bladé, R. M. Dole, D. Allured, X. Quan, P. Pegion, and J. Eischeid (2014), Understanding recent eastern horn of Africa rainfall variability and change, *J. Clim.*, *27*, 8630–8645.

Lin, H., G. Brunet, and J. Derome (2009), An observed connection between the North Atlantic Oscillation and the Madden-Julian Oscillation, *J. Clim.*, *22*, 364–380.

Manatsa, D., and S. K. Behera (2013), On the epochal strengthening in the relationship between rainfall of East Africa and IOD, *J. Clim.*, *26*, 5655–5673.

Manatsa, D., Y. Morioka, S. K. Behera, C. H. Matarira, and T. Yamagata (2014), Impact of Mascarene High variability on the East African 'short rains', *Clim. Dyn.*, *42*, 1259–1274.

Manatsa, D., C. Mudavanhu, T. D. Mushore, and E. Mavhura (2015), Linking major shifts in East Africa 'short rains' to the Southern Annular Mode, *Int. J. Climatol.*, *36*, 1590–1599, doi:10.1002/joc.4443.

Manola, I., F. M. Selten, W. P. M. de Ruijter, and W. Hazeleger (2015), The ocean-atmosphere response to wind-induced thermocline changes in the tropical South Western Indian Ocean, *Clim. Dyn.*, *45*, 989–1007.

Mutai, C., D. Polzin, and S. Hastenrath (2012), Diagnosing Kenya rainfall in boreal autumn: Further exploration, *J. Clim.*, *25*, 4323–4329.

Mutai, C. C., and M. N. Ward (2000), East African rainfall and the tropical circulation/convection on intraseasonal to interannual time scales, *J. Clim.*, *13*, 3915–3939.

Nicholson, S. E. (2015), Long-term variability of the East African 'short rains' and its links to large-scale factors, *Int. J. Climatol.*, *35*, 3979–3990.

Philippon, N., P. Camberlin, V. Moron, and J. Boyard-Micheau (2015), Anomalously wet and dry rainy seasons in equatorial East Africa and associated differences in intra-seasonal characteristics, *Clim. Dyn.*, *45*, 2101–2121.

Preethi, B., T. P. Sabin, J. A. Adedoyin, and K. Ashok (2015), Impacts of the ENSO Modoki and other tropical Indo-Pacific climate drivers on African rainfall, *Sci. Rep.*, *5*, 16653, doi:10.1038/srep16653.

Saji, N. H., B. N. Goswami, P. N. Vinayachandran, and T. Yamagata (1999), A dipole mode in the tropical Indian Ocean, *Nature*, *401*, 360–363.

Saji, N. H., S.-P. Xie, and T. Yamagata (2006), Tropical Indian Ocean variability in the IPCC 20th-century climate simulations, *J. Clim.*, *19*, 4397–4417.

Sayantani, O., and C. Gnaseelan (2015), Tropical Indian Ocean subsurface temperature variability and the forcing mechanisms, *Clim. Dyn.*, *44*, 2447–2462.

Schneider, U., A. Becker, P. Finger, A. Meyer-Christoffer, M. Ziese, and B. Rudolf (2014), GPCC's new land surface precipitation climatology based on quality-controlled in situ data and its role in quantifying the global water cycle, *Theor. Appl. Climatol.*, *115*, 15–40.

Thompson, D. W. J., and J. M. Wallace (2000), Annular modes in the extratropical circulation. Part I: Month-to-month variability, *J. Clim.*, *13*, 1000–1016.

Tozuka, T., M. Nagura, and T. Yamagata (2014), Influence of the reflected Rossby waves on the western Arabian Sea upwelling region, *J. Phys. Oceanogr.*, *44*, 1424–1438.

Ummenhofer, C. C., A. S. Gupta, M. H. England, and C. J. C. Reason (2009), Contributions of Indian Ocean sea surface temperatures to enhanced East African rainfall, *J. Clim.*, *22*, 993–1013.

Vasala, V. (2008), First and second baroclinic mode response of the tropical Indian Ocean to interannual equatorial wind anomalies, *J. Oceanogr.*, *64*, 479–494.

Watanabe, M. (2004), Asian jet waveguide and a downstream extension of the North Atlantic Oscillation, *J. Clim.*, *17*, 4674–4691.

Webber, B. G. M., A. J. Matthews, and K. J. Heywood (2010), A dynamical ocean feedback mechanism for the Madden-Julian Oscillation, *Q. J. R. Meteorol. Soc.*, *136*, 740–754.

Webber, B. G. M., A. J. Matthews, K. J. Heywood, and D. P. Stevens (2012), Ocean Rossby waves as a triggering mechanism for primary Madden-Julian events, *Q. J. R. Meteorol. Soc.*, *138*, 514–527.

Webster, P. J., A. M. Moore, J. P. Loschnigg, and R. R. Leben (1999), Coupled ocean-temperature dynamics in the Indian Ocean during 1997–98, *Nature*, *401*, 356–360.

Xie, P., and P. A. Arkin (1997), Global precipitation: A 17-year monthly analysis based on gauge observations, satellite estimates, and numerical model outputs, *Bull. Am. Meteorol. Soc.*, *78*, 2539–2558.

Xie, S.-P., H. Annamalai, F. A. Schott, and J. P. McCreary (2002), Structure and mechanisms of south Indian Ocean climate variability, *J. Clim.*, *15*, 867–878.

Xie, S.-P., K. Hu, J. Hafner, H. Tokinaga, Y. Du, G. Huang, and T. Sampe (2009), Indian Ocean capacitor effect on Indo-Western Pacific climate during the summer following El Niño, *J. Clim.*, *22*, 730–747.

Zhuang, W., M. Feng, Y. Du, A. Schiller, and D. Wang (2013), Low-frequency sea level variability in the southern Indian Ocean and its impacts on the oceanic meridional transports, *J. Geophys. Res. Oceans*, *118*, 1302–1315, doi:10.1002/jgrc.20129.

Yuan, J., S. B. Feldstein, S. Lee, and B. Tan (2011), The relationship between the North Atlantic jet and tropical convection over the Indian and western Pacific Oceans, *J. Clim.*, *24*, 6100–6113.